

Gas Injection into Second Mode Instability on a 7° Cone at Mach

7

Philipp Kerth*, Sebastien Wylie[†], Raghul Ravichandran[‡] and Matthew McGilvray[§]
Oxford Thermofluids Institute, University of Oxford, Oxford, OX2 0ES, United Kingdom

The influence of injection gas type on second mode instabilities is researched on a 7° half-angle cone at Mach 7. The wind tunnel model of 594.5 mm length with a sharp nosetip is fitted with a porous aluminium patch that spans 60° in azimuth and 25 mm in axial length. Four different gases are injected into the boundary layer flow, namely nitrogen, carbon dioxide, helium and argon. Three different tunnel test conditions with different Re_u provide a variety of amplification levels of the second mode instability at the injection location. Frequency data is obtained using PCB sensors and the density boundary layer thickness is inferred from high speed z-type schlieren images. Early analysis of initial data shows a drop in second mode frequency and second mode power behind the injector. If transition is not caused the effect weakens further downstream. Higher blowing ratios caused a stronger decrease in frequency and also reduced the power in the frequency band more. Larger blowing ratios are required at lower Re_u to achieve the same effect. The observed boundary layer thickness, as inferred from schlieren images, followed comparable dynamics. A larger blowing ratio of the same coolant gas lead to more thickening, while Helium had a significantly stronger total effect than carbon dioxide. Preliminary results suggest that helium injection at a moderate rate causes the second mode peak to be disproportionately damped and its bandpower to be significantly reduced. A strongly simplified analytical model suggest that the mechanical increase in boundary layer thickness alone may not be sufficient to explain all observed outcomes.

I. Nomenclature

A	=	Amplitude of oscillation
R_N	=	Nose radius of cone
Re_u	=	Unit Reynolds number
m	=	Molecular mass
R	=	Gas constant
γ	=	Ratio of specific heats
T	=	Temperature
f	=	Frequency
f_0	=	Undisturbed second mode frequency
FWHM	=	Full width at half maximum of a peak
PSD	=	Power spectral density
t	=	Time
M	=	Mach Number
x, y, z	=	Spatial coordinates
φ	=	Azimuth angle on cone surface
K_D	=	Darcy coefficient
K_F	=	Forchheimer coefficient
B_h	=	Blowing parameter
F	=	Blowing ratio
h	=	Boundary layer height

*PhD Candidate, Department of Engineering Science, University of Oxford

[†]Senior Postdoctoral Researcher, Department of Engineering Science, University of Oxford

[‡]PhD Candidate, Department of Engineering Science, University of Oxford

[§]Associate Professor, Department of Engineering Science, University of Oxford

δ	=	Change in boundary layer height
\dot{m}	=	Mass flow
St	=	Stanton number
e	=	Boundary layer edge properties
c	=	Injection gas properties
0	=	Uncooled properties
ent	=	Entrainment properties
w	=	Model wall properties

II. Introduction

Minimizing the heat load on hypersonic spaceplanes or re-entry vehicles is a critical challenge for hypersonic flight [1]. Boundary layer transition research has been of interest due to its overarching role in this problem for a long time. The increased heat load of a turbulent boundary layer [2] and subsequent design requirements necessitate experimental and theoretical investigations. In addition, research on gas injection in hypersonic flow environments has previously been motivated by its capability to replicate ablation (e.g. [3]) and is now of interest due to its role in active surface cooling, namely transpiration cooling (e.g.[4]). Older research in the area only provides transition location data, mostly inferred from heat transfer measurements (e.g. [5]). It is nowadays however well established that the so called second mode or Mack mode [6] is the decisive mechanism that causes transition in hypersonic boundary layers. As a result, contemporary research is additionally focused on capturing frequency data. Until the early 2000's a broad agreement was that mass addition into the boundary layer has a destabilizing effect, causing earlier transition. This is described for example by Schneider in [7]. However, during the last 20 years this has been challenged: Leyva, Fuji, Hornung and Jewell et al. [8–11] have published research on the stabilizing effect of CO₂ injection into the boundary layer. The vibrational modes of the molecule contribute to a delay in transition by absorbing some energy from the present boundary layer instabilities. Furthermore, research from DLR in the past years has suggested a strong influence of the position of injection with respect to Reynolds number and its spatial extension on its effect on stability. Camillo et al. [4, 12] observed that all studies which found a destabilizing effect had something in common: ‘mass addition in those studies was performed along a large portion of the body’ [12]. By using a smaller injector close to the expected region of transition onset they achieved a transition delay of up to 17% using nitrogen as a coolant and hence excluding the vibrational energy effects [12]. Their tests were conducted in HEG, a reflected shock tunnel at Mach 7.3 [4, 12] and a total flow enthalpy from 3.08 MJ/kg to 3.24 MJ/kg. An experiment in the VKI-H3 Mach 6 noisy blowdown tunnel with a cone including a porous section provides similar flow properties such as unit Reynolds number and total temperature as found in the University of Oxford's HDT facility [13]. Miró Miró et al. found a reduction in second mode wavenumber and an advance in transition location based on infrared data and planar laser induced fluorescence measurements. However, as also noted their injection location was far upstream of the critical N-factor and hence from the transition location [12] in comparison to the DLR cone experiments.

A numerical study by Miró Miró et al. investigated the influence of gas type on boundary layer transition. The geometry used for the simulation had a large porous surface covering most of the model. It was concluded that the increased destabilizing effect of lighter gases cannot originate from their presence in the boundary layer flow alone. Helium was found to cause a large thickening of the temperature boundary layer due to its higher thermal diffusivity, to dampen the most unstable frequency, and to also broaden the unstable frequency spectrum. Damping prevailed and hence Helium was found to have stabilizing effect, provided the gas injection is continuous across the surface. If this is not the case, then a weak shocklet was determined as the reason for advanced transition [14].

Because an entirely continuous injection area is not realistic for a transpiration cooling application, more work is necessary to investigate small porous sections. For this work, a variation of freestream unit Reynolds numbers allows different levels of instability at the injection location on a cone. A variety of different gases were injected, whilst keeping the blowing ratios comparable. In order to create a realistic case for transpiration cooling, the injection location is confined to a small area relative to the whole model.

III. Experimental Setup

A. Cone Model and Instrumentation

The model for wind tunnel testing is a 7° half-angle cone with a sharp nosetip ($R_N \approx 0.05$ mm) and a total length of 594.5 mm. The porous injector is a 60° frustum insert at 300 mm from the sharp tip as shown in Fig. 1. The cone is manufactured from stainless steel except for the rear segment and sharp nosetip which are made from 7075 T6 aluminium. Porous aluminium Metapor BF100 Al, which is manufactured by Portec [15] has been used to machine the injector insert. 19 PCB ultra high speed piezoelectric differential pressure transducers are flush mounted on the

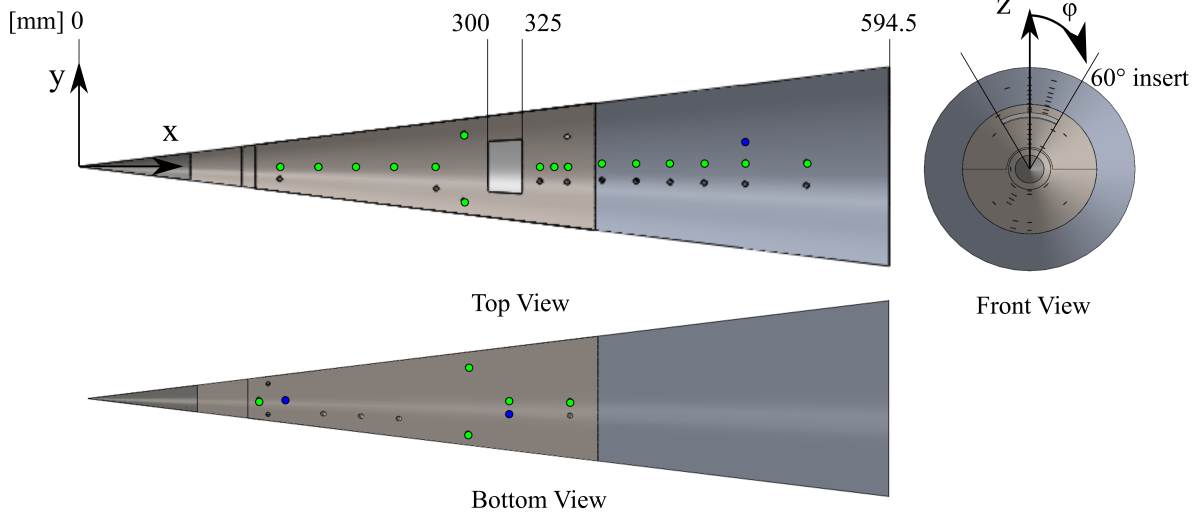


Fig. 1 Geometry of the cone model. Green: PCB, Blue: Kulites. The given coordinate system (x, y, z, ϕ) will be used in all further representations.

model surface to provide high frequency pressure data. This sensor model has been used by multiple research groups for boundary layer instability investigation such as Wylie et al. [16], Grossir et al. [17], Casper et al. [18] and Estorf et al. [19]. Types PCB132A31 and PCB132B38 are used and no noticeable difference in their frequency response was found. In addition, three Kulite XCEL-152 provide absolute pressure data for the model surface and the inside of the injection gas plenum respectively. The instrumentation types and location are shown in Figure 1.

B. Injector System

Supplying the porous injector with gas is achieved via a reservoir tank and a mass flow controller. For this application an Omega FMA2611A 250 slpm range model is chosen. Blowing ratios up to 2.0% can be attained at the investigated tunnel conditions. The repeatability is $\pm 0.2\%$ of the full scale and the accuracy of the mass flow is $\pm(0.8\% \text{ reading} + 0.2\% \text{ fullscale})$ [20]. Two main reasons motivated the choice of mass flow controllers for the application: firstly, the mass flow rate can be directly read from the MFC and can then be confirmed using the Darcy-Forchheimer equation for flow through a porous medium during a test. Secondly, precisely setting the mass flow rate for different gases should enable a high level of repeatability in between experiments while keeping the operational procedure simple. The mass flow rate \dot{m} is directly used for the calculation of the blowing ratio F .

$$F = \frac{\dot{m}_c}{\dot{m}_e} = \frac{\rho_c u_c}{\rho_e u_e} \quad (1)$$

Where the index e represents the boundary layer edge and c the properties of the injected gas. This normalization is a standard practice in literature (e.g.[12, 21, 22]). The boundary layer edge properties are hereby calculated using the Taylor-Macoll equation [23] in an iterative procedure.

Another quantitative comparable value for the amount of blowing can also be defined via St and is for example shown in

Table 1 Sensor locations on cone model. ($\varphi = 0^\circ$) corresponds to the central plane of the injector.

Hole Number	Sensor Type	x [mm]	φ [°]
PCB 1	Differential Pressure - Surface	107.0	0
PCB 2	Differential Pressure - Surface	127.0	0
PCB 3	Differential Pressure - Surface	147.0	0
PCB 4	Differential Pressure - Surface	175.0	0
PCB 5	Differential Pressure - Surface	203.0	0
PCB 6	Differential Pressure - Surface	231.0	0
PCB 7	Differential Pressure - Surface	262.0	0
PCB 8	Differential Pressure - Surface	338.0	0
PCB 9	Differential Pressure - Surface	348.0	0
PCB 10	Differential Pressure - Surface	358.0	0
PCB 11	Differential Pressure - Surface	282.0	45
PCB 12	Differential Pressure - Surface	282.0	315
PCB 13	Differential Pressure - Surface	282.0	135
PCB 14	Differential Pressure - Surface	282.0	225
PCB 15	Differential Pressure - Surface	312.5	180
PCB 16	Differential Pressure - Surface	358.0	180
PCB 17	Differential Pressure - Surface	383.7	0
PCB 18	Differential Pressure - Surface	408.7	0
PCB 19	Differential Pressure - Surface	433.7	0
PCB 20	Differential Pressure - Surface	458.7	0
PCB 21	Differential Pressure - Surface	488.7	0
PCB 22	Differential Pressure - Surface	533.7	0
Ku 1	Absolute Pressure - Surface	145.0	180
Ku 2	Absolute Pressure - Surface	312.5	180
Ku 3	Absolute Pressure - Surface	388.7	330
Ku 4	Absolute Pressure - Plenum	N/A	N/A

[24, 25]:

$$B_h = \frac{F}{St_0} \quad (2)$$

Hereby, St_0 is obtained via a laminar Eckert reference enthalpy calculation [26] using the Chilton Colburn analogy factor [27] and the viscosity models from Keyes [28] and Sutherland [29]. The given St_0 is then adapted for a cone by multiplication with $\sqrt{3}$ according to the Mangler transformation [30, 31]. Both injectors are manufactured from porous aluminium METAPOR BF100A1. The outflow characteristics are determined using the method described in Ref. [32, 33] based on a Nelder-Mead algorithm [34] and carried out using Matlab's inbuilt `FMINSEARCH` function [35]. The Darcy-Forchheimer coefficients were found to be $K_D = (4.2 \pm 0.1) \times 10^{-12} \text{ m}^2$ and $K_F = (1.14 \pm 0.01) \times 10^{-8} \text{ m}$ within 95 % confidence. The porous material in use might have an inhomogeneous distribution of porosity, or leaks might be present at the interfaces of porous injector and surrounding stainless steel. The outflow is hence characterized using a hot-wire probe. Due to the curved shape of the injectors, the probe tip is moved across the frustum injector patch using a five-axis traverse system. This way, the hot-wire probe is kept at a constant distance to the porous material of 1.5 mm while the mounting arm is kept surface normal to minimize flow interactions. Velocity values are recorded as an average over three seconds at every location and buffer time in between the measurements minimizes disturbances to the flow due to the traverse readjustment. During the entire test time the mass flow rate is kept constant by a mass flow controller Omega FMA2609A. Results can be seen in Figure 2 for the frustum. A total of 500 points were measured along the surface, with 20 columns along the 25 mm axial length of the injector and 25 rows spanning $-35^\circ \leq \varphi \leq 35^\circ$.

The flow rate was kept at 3.0 slpm. Miró Miró et al. characterized their injector using a pitot tube and found that one of

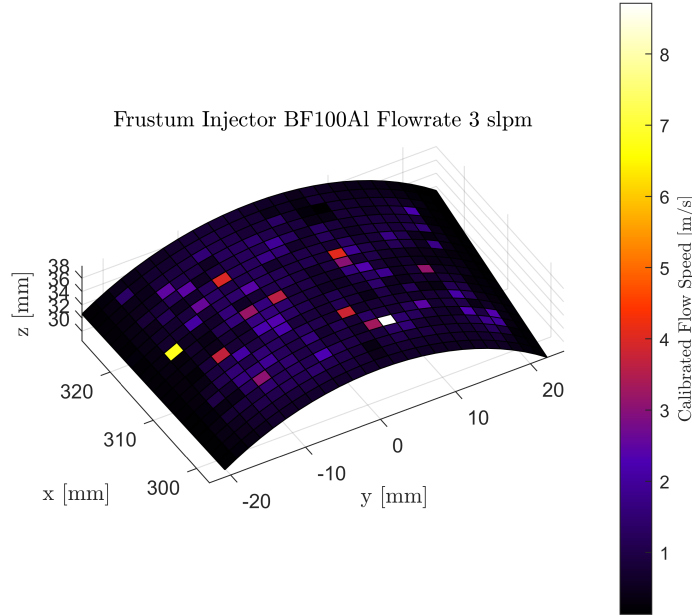


Fig. 2 Howire outflow measurement at atmospheric pressure.

their injector geometries exhibited substantial inhomogeneities. However, when comparing it to a more homogeneous case they found no difference in the downstream effect of the injection [13]. As those tests were conducted in a noisy blowdown tunnel and had pore sizes an order of magnitude higher than BF100A1, more research is necessary to conclude the effect of blowing inhomogeneities in HDT on boundary layer transition experiments.

C. Oxford High Density Tunnel and Test Conditions

Measurements are conducted in the Oxford High Density Tunnel (HDT) at Mach 7 operating the facility as a Ludwieg Tube. The tunnel consists of a 17.4 m long Ludwieg tube, a fast acting plug-valve, gate valve and a converging/diverging nozzle. It has been commissioned by Wylie et al. for boundary layer experiments at Mach 7 by comparing its results to DLR H2K facility [36, 37]. Additional information about the facility design can be found in Refs. [36, 37].

The range of Reynolds numbers while keeping the nose radius constant will allow control of the boundary layer stability over the cone model. Multiple cases are hence investigated. Ranging from a turbulent boundary layer at the location of the injector to slowly growing second modes. Data is recorded at 2 MHz using a NI PXIe-1082 data acquisition system

Table 2 Flow properties for the HDT Conditions.

Cond. No.	P_{fill} [kPa]	T_{fill} [K]	T_{tot} [K]	M	T_{stat} [K]	Re_u [$10^6/m$]	p_{stat} [Pa]	p_{stag} [kPa]
1	2485	500	410 ± 15	7.0	38	13.1	475 ± 20	1820
2	1400	500	410 ± 10	6.9	38	7.5	280 ± 20	1030
3	3500	500	410 ± 10	7.0	37	18.7	665 ± 20	2570

and different amplifiers for each sensor type respectively. The Kulite signals are processed by a FYLDE transducer amplifier, the PCB sensors by a PCB 483C15 series signal conditioner.

All experiments are conducted at zero degrees angle of attack, with the cone model mounted on an automated traverse mechanism to allow alignment of the model to $\pm 0.1^\circ$. The alignment procedure is carried out using frequency measurements at four different azimuthal positions and the same axial location. The model is considered aligned, when the frequency of the second mode instability match.

IV. Influence of Injection on Second Mode Frequencies

A. Data Analysis Procedure

Characteristics of the second mode are investigated using frequency data obtained from PCB sensors. A power spectral density is then calculated using Welch's PSD estimate [38, 39] with a Hann window of 50% overlap [40, 41]. An example for this can be seen in Figure 3. The investigated tunnel conditions show either strongly amplified second modes at the injection location (Condition 1, $Re_u = 13 \cdot 10^6/m$) or initial growth of instabilities (Condition 2, $Re_u = 7.5 \cdot 10^6/m$). For Condition 3 ($Re_u = 18.7 \cdot 10^6/m$) there is still a peak in the second mode frequency region present, even though the large amplitude in lower frequency regions suggests transition has already begun. PCB15 is located at $x = 312.5$ mm, $\varphi = 180^\circ$ and hence at the opposite side of the porous injector location. During those shots, no coolant injection was present. A resonance frequency and electrical noise peak that is also found in the pre-trigger

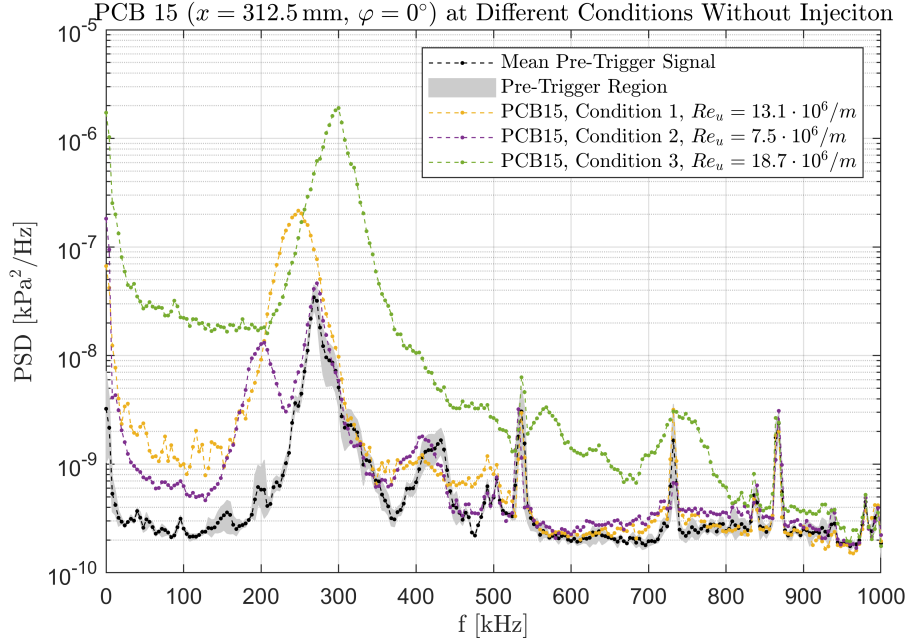


Fig. 3 PSD of three conditions used during the testing.

signal, where no flow is present over the sensor, lies closely to the expected value of the second mode. In the shown examples the signal during the flow lies either about an order of magnitude above the signal or the frequency peaks are at different locations. This is however not true for all sensors and all conditions. In order to investigate the development of the second mode characteristic frequency peak via its centre, FWHM and amplitude it is necessary to remove this artefact. A fitting procedure is hence applied aiming to remove the peak caused by the resonance and recovering the true second mode signal [42, 43]. It is assumed that all peaks can be fitted with a Gaussian distribution which is following the approach seen in Ref. [12]. The fits are carried out using a least square method from Python's *scipy* package [44, 45]. An example of the fitting results can be seen in Figure 4. It can be inferred from the plots that the carbon dioxide injection visibly alters the second mode frequency spectrum. For this work, two main parameters are selected to characterize those changes, namely the central frequency and the power carried in the spectrum. For the frequency characteristics the value of f/f_0 will be plotted, where f_0 is the frequency at the same sensor location without any injection present. For the shown amplitudes of the second mode, Matlab's *bandpower* function is applied to the PSDs from 100 kHz to 400 kHz. The bandpower from the same interval in the pre-trigger signal is subtracted. The boundaries are held at this constant value to provide comparability between conditions. As Figure 3 shows for Condition 3, upon transition onset a rise in low frequency content gradually covers the second mode. This has the potential to influence the signal to background level of the second mode peak to a prohibitive extent. For this reason, a fit is only performed to the sensor if the second mode peak can be identified unambiguously.

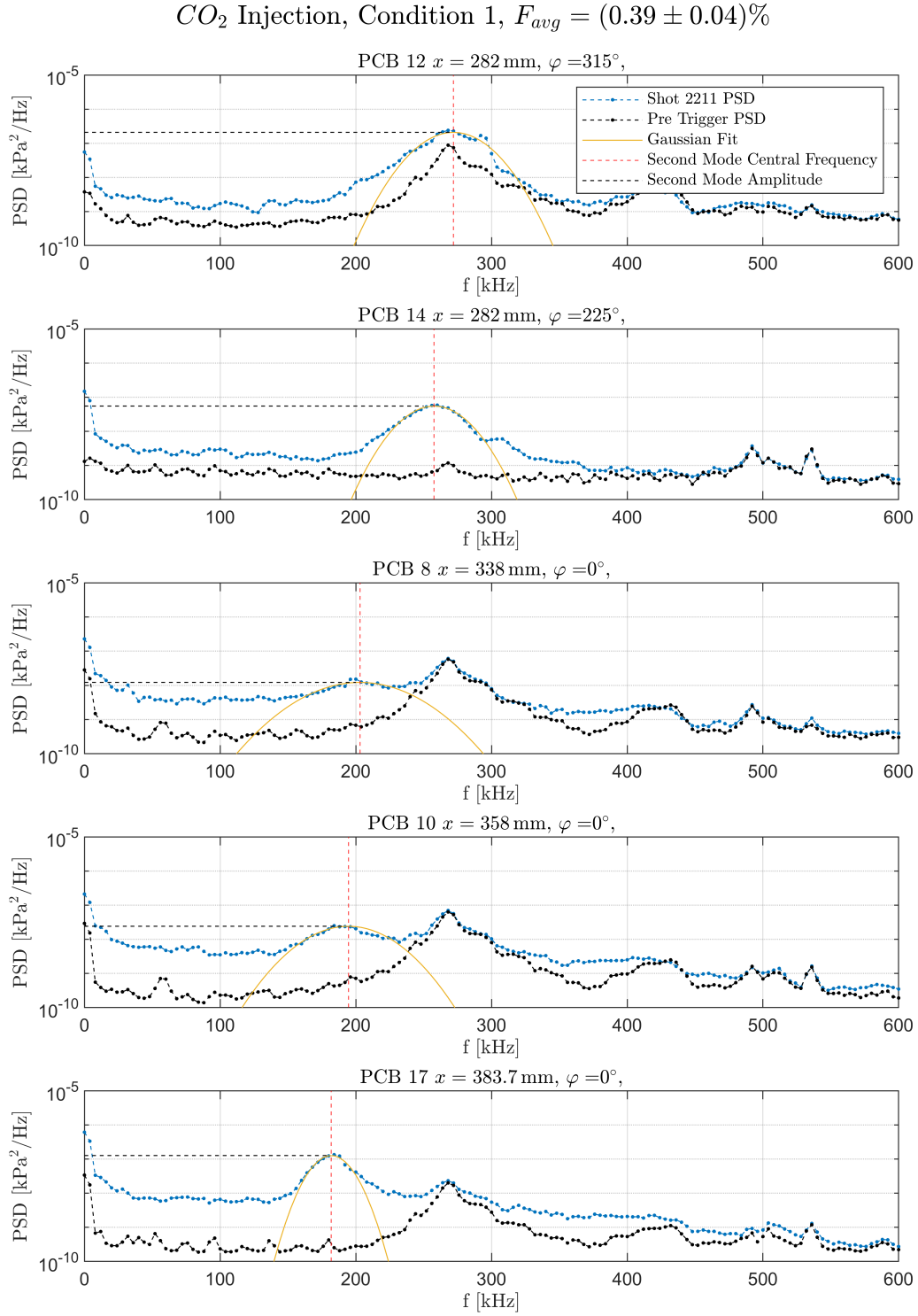


Fig. 4 Applied fits to PSD data. PCB 11 and 13 are upstream of the injector, while PCB8, PCB10 and PCB17 are downstream.

B. Experimental Results

1. Frequency Development without Injection

Tracking the central frequency of the second mode gives insight into behaviour of the mechanism leading to transition. As shown in Figure 5 the second mode frequency without any injection decreases steadily downstream. For Condition 1, the sensors with $x > 470$ mm already showed an increase in low frequency content, making the fitting procedure less reliable. The points with $x > 470$ mm are therefore excluded. The increase can be explained due to the increase in boundary layer thickness downstream. The frequency of the second mode is therefore expected to be lower for $Re_u = 7.5 \cdot 10^6/m$ than for $Re_u = 13.1 \cdot 10^6/m$. Those baseline frequency parameters will now be used as f_0 in all further plots. Symbols represent the conditions or blowing ratios, colors the coolant gases and the values of F are given in the figure legends.

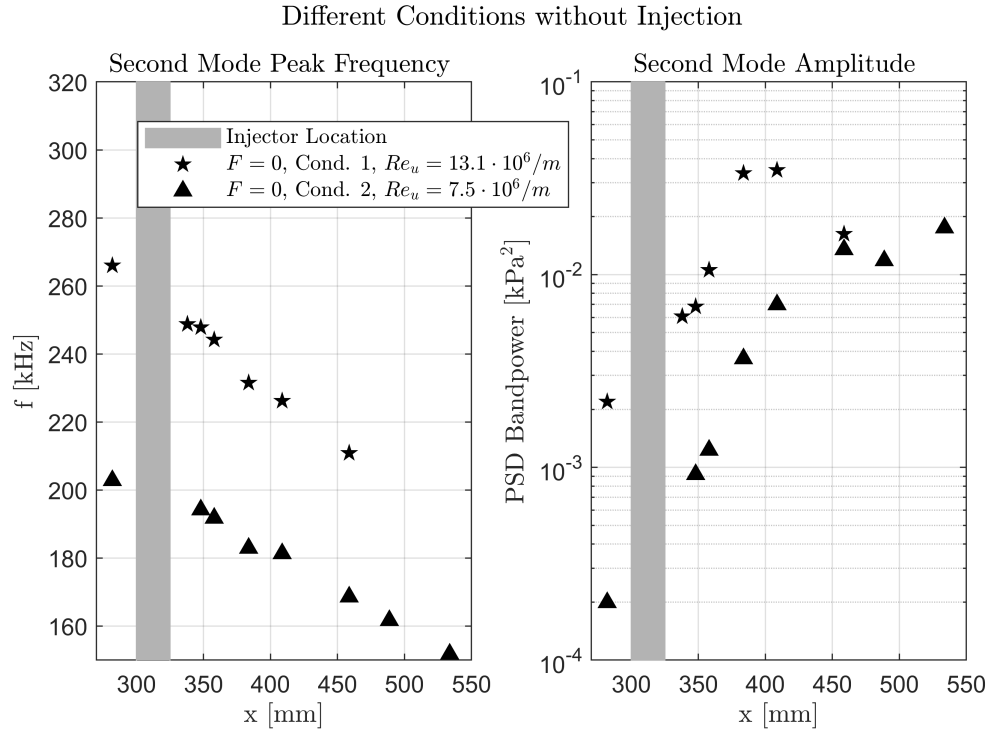


Fig. 5 Condition 1 and 2 second mode development without injection.

2. Moderate Reynolds Number - $Re_u \approx 13.1 \cdot 10^6/m$

When gases are injected into the boundary layer the power and frequency of the second mode are reduced. For carbon dioxide, argon and nitrogen a higher blowing ratio means a larger reduction (see Figure 6). For $F \approx 0.35\%$ the effects of CO_2 and Ar is comparable. It is however unclear at this point why the shots with Ar, $F \approx 0.12$ and N_2 , $F \approx 0.22$ show a disproportionally larger effect on the second mode frequency. In contrast to all other gases, helium appears to cause a frequency increase further downstream. At higher blowing ratio, the frequency peaks in the second mode spectra were damped very significantly, the fitting procedure could only be performed at one sensor at $x = 383.7$ mm, $\varphi = 0^\circ$. For the spectral power, helium also shows a unique effect among the gases. Especially downstream of 400 mm, the power is significantly lower than for other coolant gases and the undisturbed case. The values only approach the shot without injection at the most downstream sensor. This requires further investigation and individual power spectra can be found in Section IV.C.

Condition 1, $M = 7$, $Re_{unit} \approx 13.2 \times 10^6/m$, $R_N = 0.05$ mm

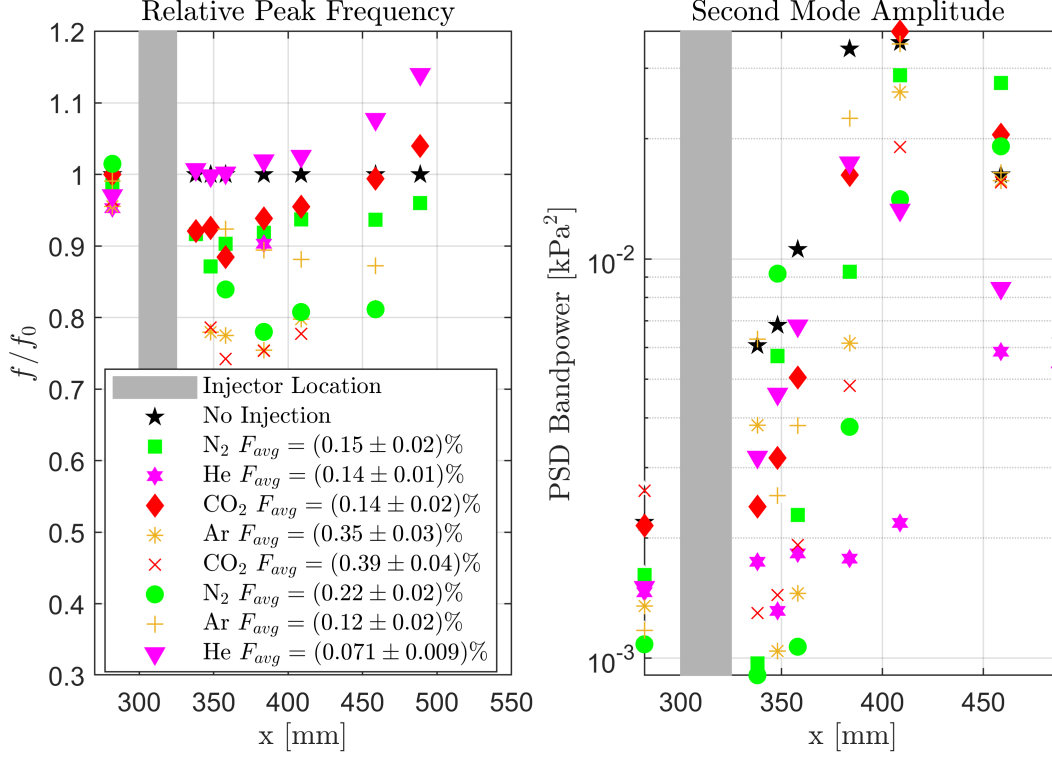


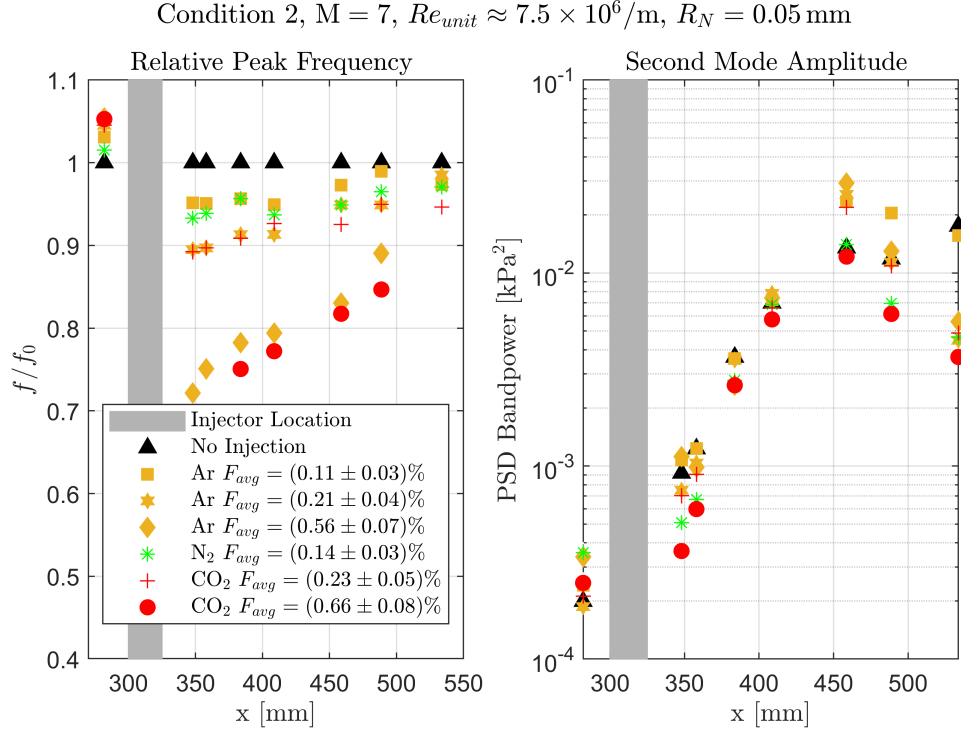
Fig. 6 Condition 1 second mode properties for various gases and blowing ratios.

3. Low Reynolds Number - $Re_u \approx 7.5 \cdot 10^6/m$

At the condition shown in Figure 7 (Condition 2), slowly amplifying second modes were present at the location of the injector (see Figure 3). The coolant flow from the porous material causes the frequency of the observed second mode peak to drop by up to 28 % for argon. At PCB 8, which is 13 mm downstream of the injector, the PSD profile was altered to a degree where the second mode peak could no longer be recognized and no fit Gaussian fit was calculated. Those points are hence not shown in the plot. For this Re_u no clear dependency of the second mode characteristics on gas type could be observed. The frequency drop is comparable for carbon dioxide and argon at similar blowing ratios. The same is true for argon and nitrogen at $F \approx 0.14$ %. In contrast, the behaviour of f/f_0 seems to be strongly dependent on the blowing ratio itself. This can clearly be seen for all three argon and both carbon dioxide cases that are shown. The power in the frequency band surrounding the second mode shows slightly different dynamics. Just downstream of the injector carbon dioxide and nitrogen show the strongest reduction in power despite the second mode frequency not being affected to a similar degree. However, the trend is not as permanent further downstream. For both conditions the second mode parameters slowly approach the undisturbed values further downstream. An explanation for this could be increased mixing of the coolant gases.

C. Helium Injection

Despite the comparably low blowing ratios helium injection had a unique effect on the second mode characteristics. For condition 1 and $F_{avg}^{He} = 0.14$ % the PSD was changed too significantly to still recognize a second mode peak and perform the fitting procedure. It is consequently necessary to investigate the individual PSD traces. Injection gases other than helium had a similar effect at moderate and low blowing ratios: The second mode peak was shifted to lower frequencies and also lost total height causing a reduction in bandpower. This is for example shown in Figure 4 for carbon dioxide. During the experiments, it was found that only blowing ratios exceeding 0.5 % at condition 1 disturb the boundary layer flow to such an extent that no second mode could be recognized anymore in the PSD. Those cases are accompanied by an instantaneous rise in low frequency content similar as in Figure 3 for $Re_u = 18.7 \cdot 10^6/m$



indicating a turbulent frequency spectrum. In contrast, minimal helium blowing caused the second mode peak to shrink disproportionately without causing a strong rise in low frequency content. This is shown in Figure 8. Plotted in blue is the shot with $F_{avg}^{He} = 0.14\%$, showing a substantial reduction of power in the frequency band around the usual second mode peaks. This effect is particularly present at the sensors with locations downstream of $x = 358$ mm. It is also notable how the low frequency content $f < 170$ kHz follows the order of the blowing ratios reciprocally for all sensors downstream of the injector once it starts rising.

In the simulation work from Miró Miró et al., where injection was applied along a large portion of a cone, it is predicted that helium would dampen the most unstable frequencies while exciting a broader spectrum of instabilities [14]. Miró Miró et al. theorize that the second mode may no longer be the driving factor of transition if helium is injected at a sufficient rate [14]. They however quickly dismiss this inference.

The bandpower shown in Figures 6 and 7 is a cumulative value representing the entire range from 100 kHz to 400 kHz. In view of the values shown in Figure 6 for this helium experiment, there seems to be a significant deviation from the usual amplification and growth process of the instability. Up to the point of a nearly turbulent frequency spectrum there is almost an order of magnitude difference in spectral power between the uncooled case and helium injection. The shown initial PSD analysis might be insufficient to capture the growth of a broadened instability spectrum, if such an effect is present. Ref. [14] does not provide second mode frequency spectra for discontinuous injection geometries, which makes the comparison of f/f_0 plots less feasible.

D. Frequency Drop and Flow Characteristics

All previous figures showed the spatial development of the second mode downstream of the injector for several different gases. For each comparison, the tunnel condition and, as far as possible, the blowing ratio were kept constant and comparable. As different tunnel conditions lead to a variety of changing boundary layer characteristics, Figure 9 attempts to draw conclusions between tunnel conditions and blowing ratios. For three different normalization parameters the relative peak frequency is shown downstream of the injector. The non-blowing cases for Conditions 1 and 2 (in black) align at $F = 0$ and $f/f_0 = 1$ due to their role as references for the calculated relative frequencies. The blowing parameter B_h , which is calculated according to the procedure described in Section III.B is multiplied by the square

Helium Injection - Power Spectral Densities

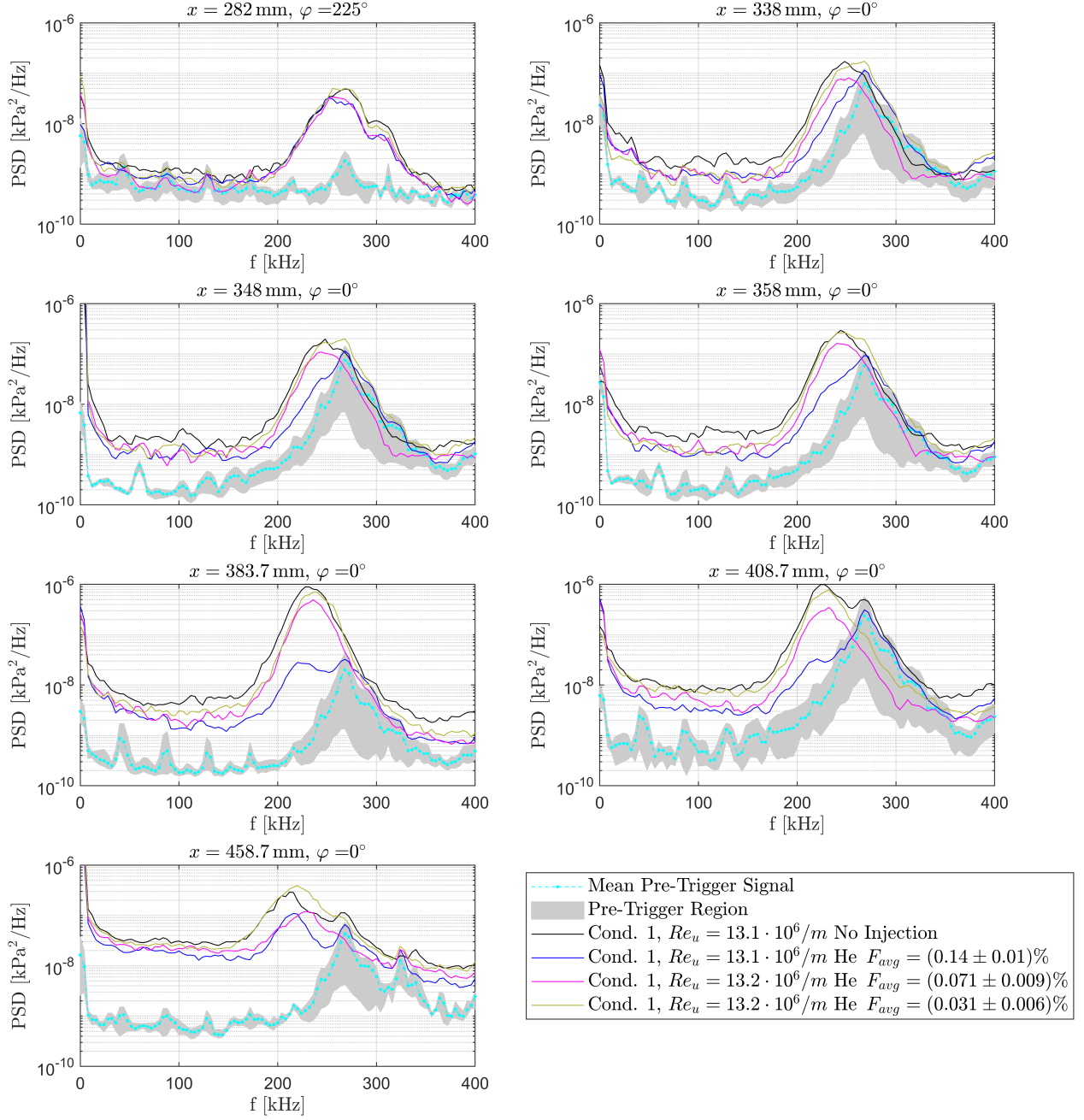


Fig. 8 PSDs for helium injection at condition 1.

root of the normalized molar mass of the coolant gas in an attempt to consider the molecular weight of the injection gas. Hereby, $M_e = 28.9583 \text{ g/mol}$ is used as the molecular mass of dry air [46] in the freestream. The shown data underlines the trend seen for helium as a coolant previously. The effect on the second mode frequency is minimal, if present at all. It is also observed, that a higher blowing ratio is necessary for Condition 2 to achieve the same relative frequency reduction as in Condition 1 using the same coolant gas. Due to the lower Re_u the boundary layer thickness should be larger for Condition 2, which may offer an explanation for this effect. This seems to be accounted for by the Reynolds number dependency of the Stanton number used in the blowing parameter. Introducing a model for coolant concentration in the boundary layer proposed by Ifti et al. [47, 48] it can be seen that the blowing parameter based

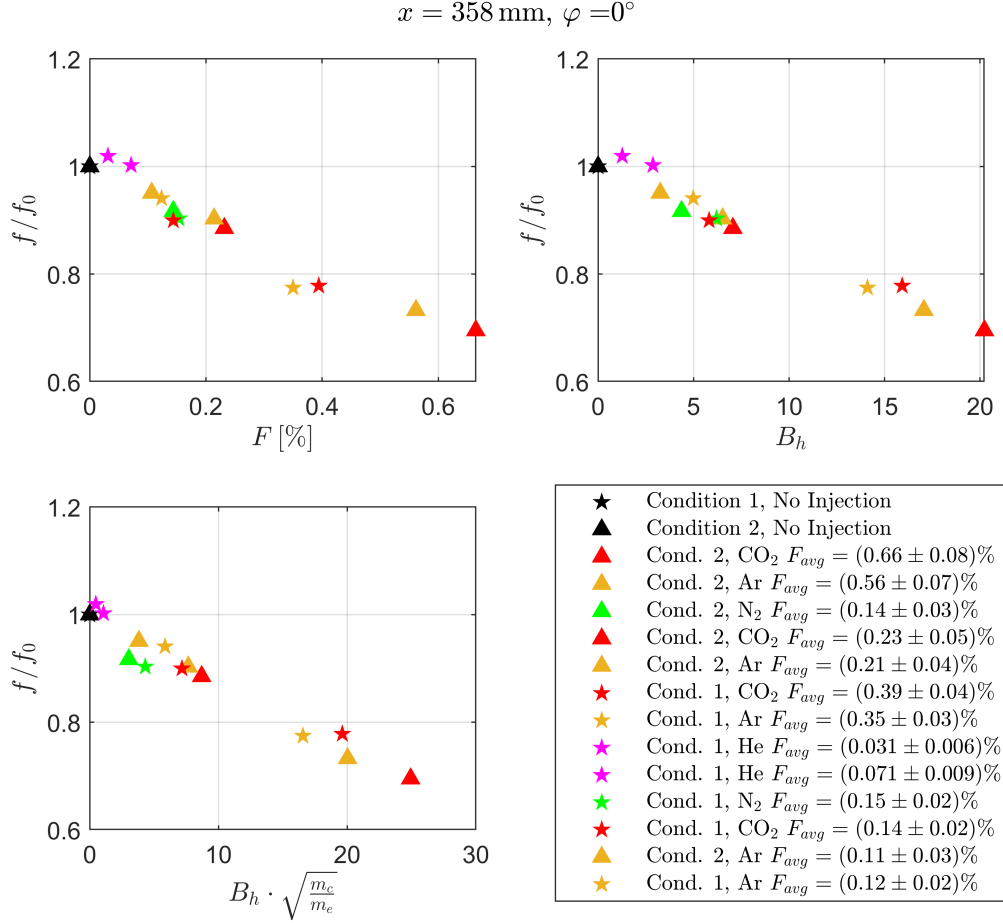


Fig. 9 Comparison of relative frequency drop for several conditions, gases and blowing ratios.

normalization is indirectly related to the boundary layer height. The boundary layer thickness increase due to the coolant outgassing shown in Figure 10 can be expressed as shown in Equation 3 which is taken from Refs. [47, 48]. Hereby, the length of the axial injector s as well as the wall-to-edge temperature ratio can be assumed as constants. Little change is found in the static temperature across tunnel conditions and hence the boundary layer edge temperature (see Table 2) can be thought of as constant. Due to the low enthalpy in the tunnel flow, model wall temperatures changes are negligible in HDT and $T_w = \text{const.}$ is room temperature. When only comparing data points of the same tunnel condition, the entrainment thickness δ_{ent} should not play a role in the proportionalities. The meaning of this additional thickness is demonstrated in Figure 10.

$$h = h' + \delta_{ent} = \frac{m_e T_w}{m_c T_e} F s + \delta_{ent}(Re, s) \quad (3)$$

A rough estimation of the second mode frequency can be made by calculating the wavelength using the waveguide thickness. It is then $f = u_e/(2h)$ [17]. Using strong simplification, those considerations leave a dependency of f/f_0 to the blowing ratio F and the normalized coolant molecular mass during the experiments. The analytical model combined with the frequency estimation for second modes suggests the following proportionalities:

$$\frac{f}{f_0} \sim \frac{1}{F} \sim \frac{m_c}{m_e} \quad (4)$$

The analytical approach correctly predicts that higher blowing ratios yield a larger drop in frequency using the same coolant. Regarding the upper left curve in Figure 9 this holds true and seems relatively independent of the injection gas type. When considering the molar mass of the injection gas, a lighter gas should cause a stronger frequency drop at the same blowing ratio. This is not found in the experiment and hence a compensating effect needs to be present. It can be

hypothesized that the local speed of sound must play a role. If one uses [49]

$$a = \sqrt{\gamma(R/m)T} \quad (5)$$

and then assumes that the effective boundary layer height scales with the local speed of sound, this still yields a square root proportionality:

$$\frac{f}{f_0} \sim \sqrt{\frac{m_c}{m_e}} \quad (6)$$

When the molecular mass of the coolant gas is taken into consideration in the lower left plot of Figure 9, a mismatch of the direct proportionalities of these overly simplistic models is evident. The lighter gases are now further away from following the relationship outlined by the proportionalities. Different effects than only the boundary layer thickness have to play a role. This might be the temperature profile, an altered velocity profile or mixing effects.

Most of the shown results are consistent with Camillo et al. experiments [12], where nitrogen also caused a reduction in second mode frequency downstream of the injector. The presented findings are however in strong contrast to the work of Schmidt et al. in their experimental investigation of a conical and cylindrical injector section on a 5° half-angle cone at Mach 4 [50, 51] which might be due to the difference in speed regime.

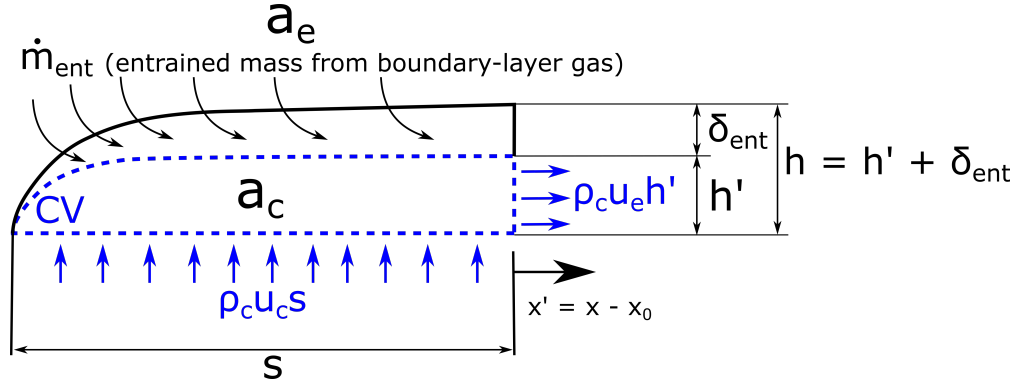


Fig. 10 Model for the coolant wall concentration above and downstream of a porous injector. Adapted from [47, 48].

V. Schlieren Measurements - Boundary Layer Thickness

The pressure measurements on the cone surface were accompanied by the operation of a z-type schlieren system. Those imaging techniques have been around for centuries, with most of the modern versions originally invented by Toepler using a knife edge [52–54] and have been used by multiple experimentalists in hypersonic wind tunnel testing [55]. Schlieren images were recorded with either a Photron AX200 Mini at 12500 fps and 57600 fps or with a Kirana 5M high speed camera at 500,000 fps. To achieve such high frame rates a Cavilux Smart UHS laser provides light at pulses of 15 ns length which were synchronized with the camera operation. The position of the image relative to the cone model as well as the resolution in pixel per mm is calibrated using a recognizable object in the image. The resolution of all images was in the order of 6.5 px/mm. The cone was rotated to $\varphi = 15^\circ$ in order to capture the side of the injector. The image plane does thus not correspond to the central array of PCB sensors. Due to the whole schlieren system being inclined by roughly 7° the knife edge was parallel to the cone. Density gradients normal to the model surface can hence be imaged as intensity changes on the camera sensor. Those gradients seen in the images were found to show a very sharp separation of boundary layer and post-shock flow. Even though it might not represent the boundary layer thickness with respect to velocity, such a thickness might deliver insights into the relationship of second mode frequency, injection and boundary layer edge. A data analysis procedure is hence applied to obtain quantitative values for the development of the density boundary layer thickness:

For comparability, a background image, taken without flow present is subtracted from every individual schlieren image. To account for possible deviations in light intensity every image is then scaled to the same background intensity. An averaged background as well as all schlieren images of the video during the shot are then subjected to an edge detection algorithm. A partial area effect based algorithm is used in Matlab [56, 57] and the procedure is shown exemplary in

Figure 11. The cone edge is inferred by using an averaged linear fit of a selected edge in the background image and a flow image. A part of the detected boundary layer edge is then selected manually for one image of the shot. An additional algorithm then collects as many points as possible along the same edge. This procedure is repeated for 100 images during a test duration with steady flow properties. All of the collected edge data points are used to calculate boundary layer thicknesses relative to the fitted cone edge. Lastly, those thicknesses are converted into physical units and transformed into the cone coordinate system. The data is binned to a resolution of 1 mm which allows statistical averaging of every value. The errorbars shown represent the mentioned statistical uncertainty as well as the propagated systematic error from the spatial image calibration and the precision of the cone edge detection. The spike visible in every trace just downstream of the injector at $x \approx 327$ mm is due to an image artefact most likely caused by the tunnel windows.

Results for carbon dioxide injection during Condition 2 are shown in Figure 12. The increase in thickness only starts

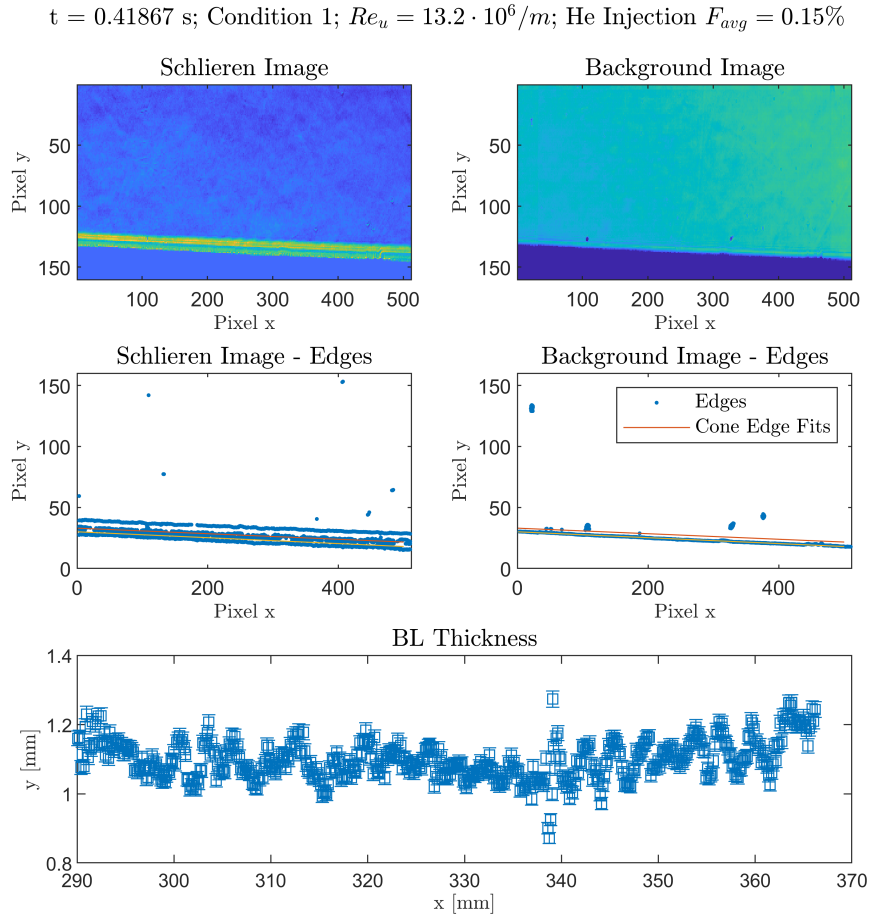


Fig. 11 Schlieren Analysis Procedure for a single image.

to be visible at around 305 mm, which can however be explained by the measured outflow profile of the injector in Section III.B, where it is shown that the majority of the outflow takes place only downstream of the front edge of the porous insert. A dependency of F and boundary layer thickness across the injector is evident for carbon dioxide as a coolant gas. In the shown case of $F_{avg} = 1.2\%$ the boundary layer was already transitioning, as shown by the downstream PCB frequency content during the test. A comparison of helium and carbon dioxide can be seen in Figure 13. Similar blowing ratios lead to a distinct difference in the detected boundary layer edge geometry. In agreement with the simulations in Ref. [14] and also the analytical model described in Section IV.D [47, 48] helium causes a disproportionally large effect on the boundary layer thickness. The plot symbols in Figure 13 correspond to the ones in

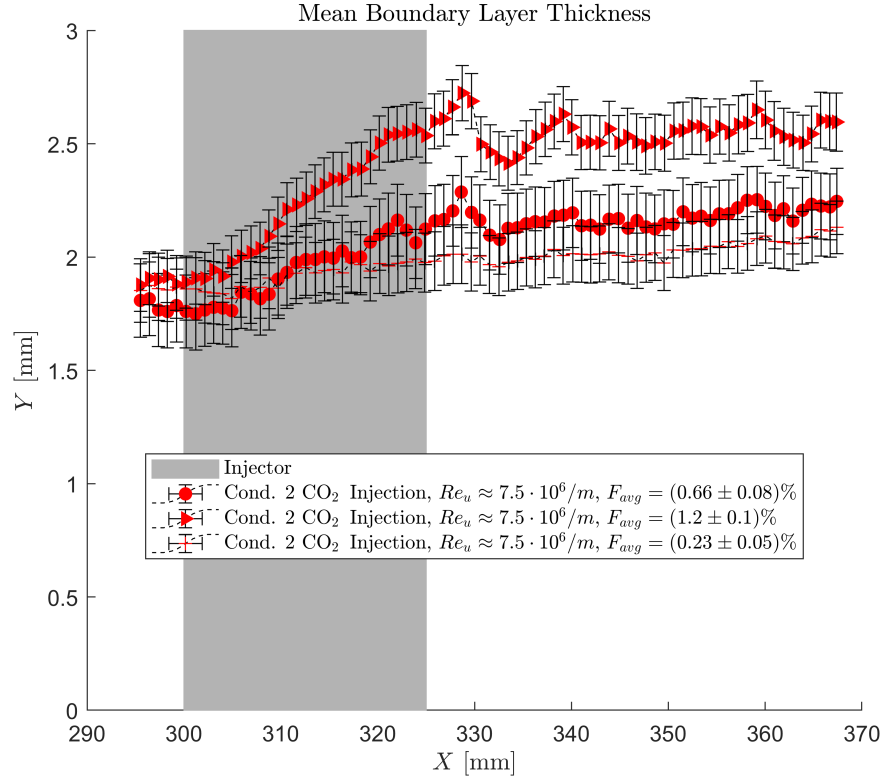


Fig. 12 Boundary layer edge thickness for carbon dioxide injection, Condition 2.

Figure 6 and considering the frequency and power behaviour for the second mode of all three shots this suggest there are other effects present than only a thickness increase of the boundary layer. These preliminary results propose a likely gas dependent mechanism that accompanies the thickness increase to explain the frequency findings in combination with the boundary layer edge geometry. Further research is hence necessary to determine what physical properties or measurement techniques could play a role.

For completeness, the raw schlieren data is shown in Figures 14 and 15. Those images are an average of the 100 frames used in the thickness calculation algorithm. The background has been subtracted and all images within one figure are normalized by the intensity of a line of pixels within the boundary layer. A change of boundary layer thickness is evident in all images showing injection cases. According to Refs. [58, 59] the sonic line distance is the relevant parameter for the second mode waveguide thickness that could be used to make predictions about the observed frequencies. As a result, the gathered data of optical density measurements can not yet be used for this purpose.

VI. Conclusion

A 7° half-angle cone with a porous injector was tested at multiple conditions in the Oxford High Density Tunnel at $M = 7$. The second mode was characterized by applying a fitting procedure to power spectral densities obtained from high frequency piezo-electric PCB sensors. We report a reduction of the second mode frequency downstream of gas injection with a strong dependency on the blowing ratio. Higher injection rates led to a stronger drop in frequency, except for helium. The frequency analysis with the initial methods was inconclusive for moderate blowing ratios. The second mode spectra were highly affected and the power in the usual frequency band was greatly reduced. Heavier injection gases did not reduce the power of the second mode to such an extent. Increased injection rates led to earlier transition as inferred by low frequency PCB data, however more research is necessary to conclude how the destabilization of the boundary layer changes with coolant gas type. Further downstream of the injector, the mass addition effect on second mode characteristics weakens and the physical parameters approach the undisturbed values. This might be due

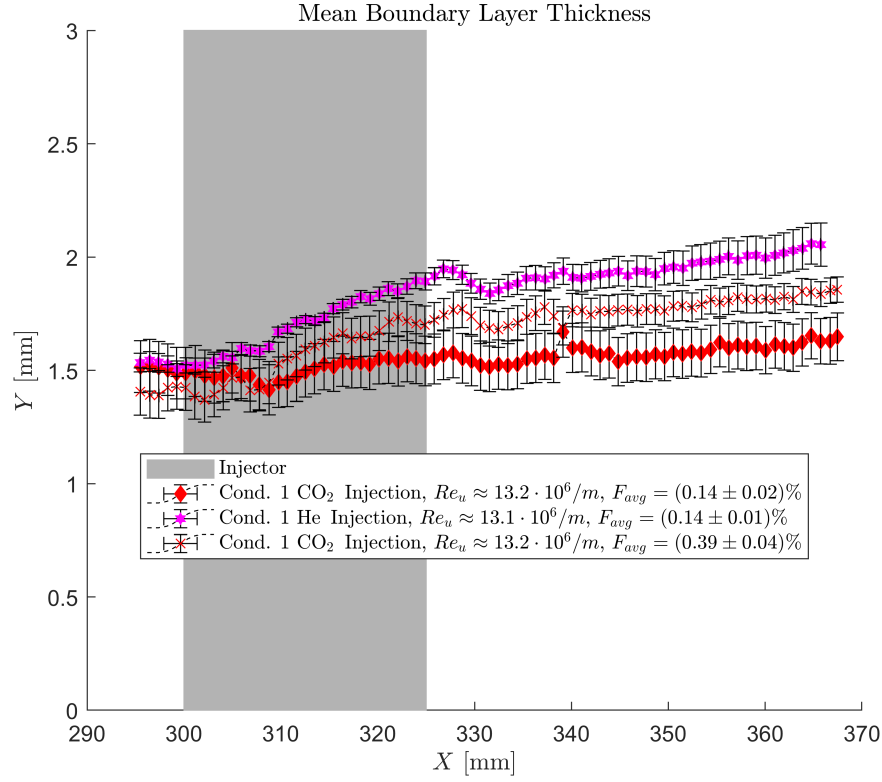


Fig. 13 Boundary layer edge thickness for carbon dioxide injection, Condition 1.

to increased mixing. Comparison to a simplified mixing model has not yet produced coherent results for the influence of injection gas molar mass. It can however attempt to explain the increase in boundary layer thickness and its effect on the second mode frequency via the wavelength in the waveguide. Schlieren images support this finding. Helium causes a much larger thickening of the density boundary layer than carbon dioxide. This underline the necessity of further investigation: The thickness increase alone does not explain the difference in spectral densities found across injection gases. For carbon dioxide alone, the thickening was directly related to F and this reiterates the matching findings from the analytical model and the experiments of the inverse proportionality of F and f/f_0 .

An inhomogeneity in the injector patch has been found and may have influenced the results. This shows, that despite a small pore size it is not always justified to assume a homogeneous outflow profile from a microporous medium. It is hence necessary to confirm the validity of the findings with improved injection uniformity across the porous insert.

VII. Acknowledgements

We particularly to acknowledge the effort of our workshop technicians David O'Dell and Duncan Blake for machining the cone model. In addition, thank you to Maxime Dahmani Moussa for the help as tunnel operator and to Eric Hembling for your continued support on the Schlieren system during the test campaign. The first author would like to thank the Rhodes Trust for their continued support. My stay at the Oxford Thermofluids Institute would not have possible without it. We acknowledge the EPSRC EP/P000878/1 research grant for their generous support of research in the field of hypersonic transpiration cooling and hence enabling this experimental work.

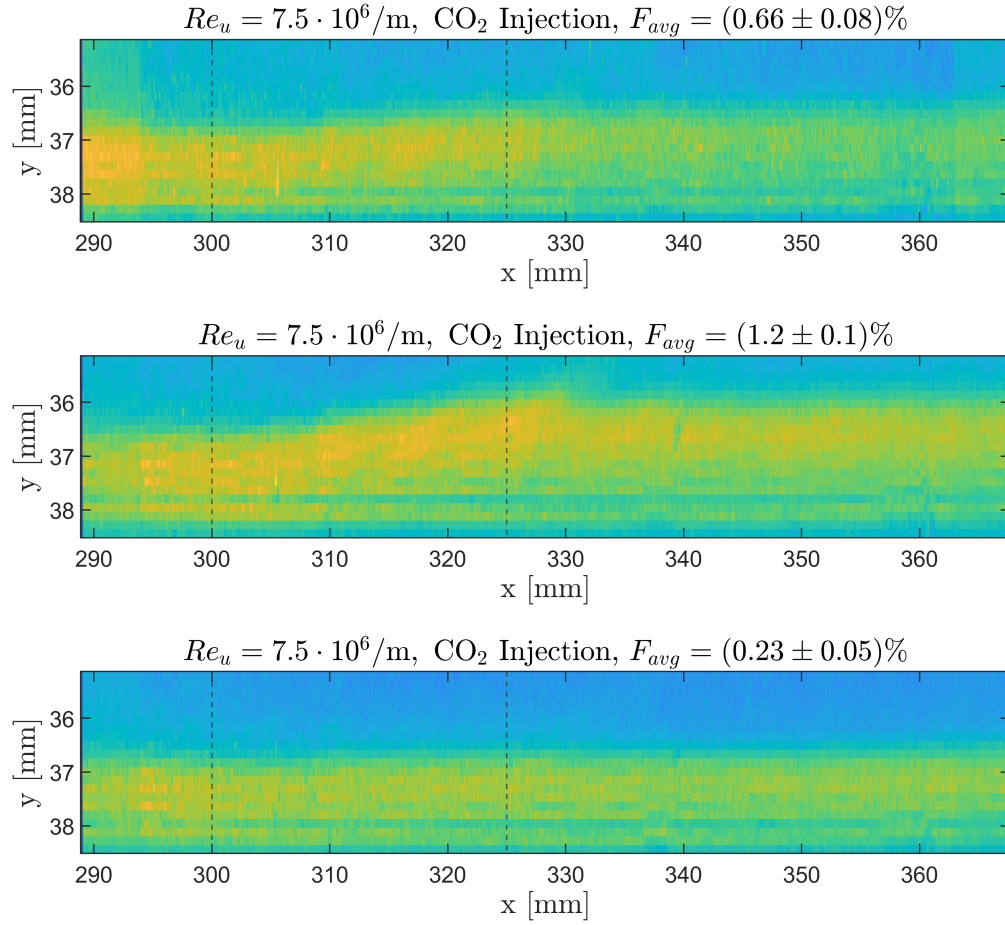


Fig. 14 Averaged schlieren images corresponding to Figure 12. Location of the injector is indicated with dashed lines.

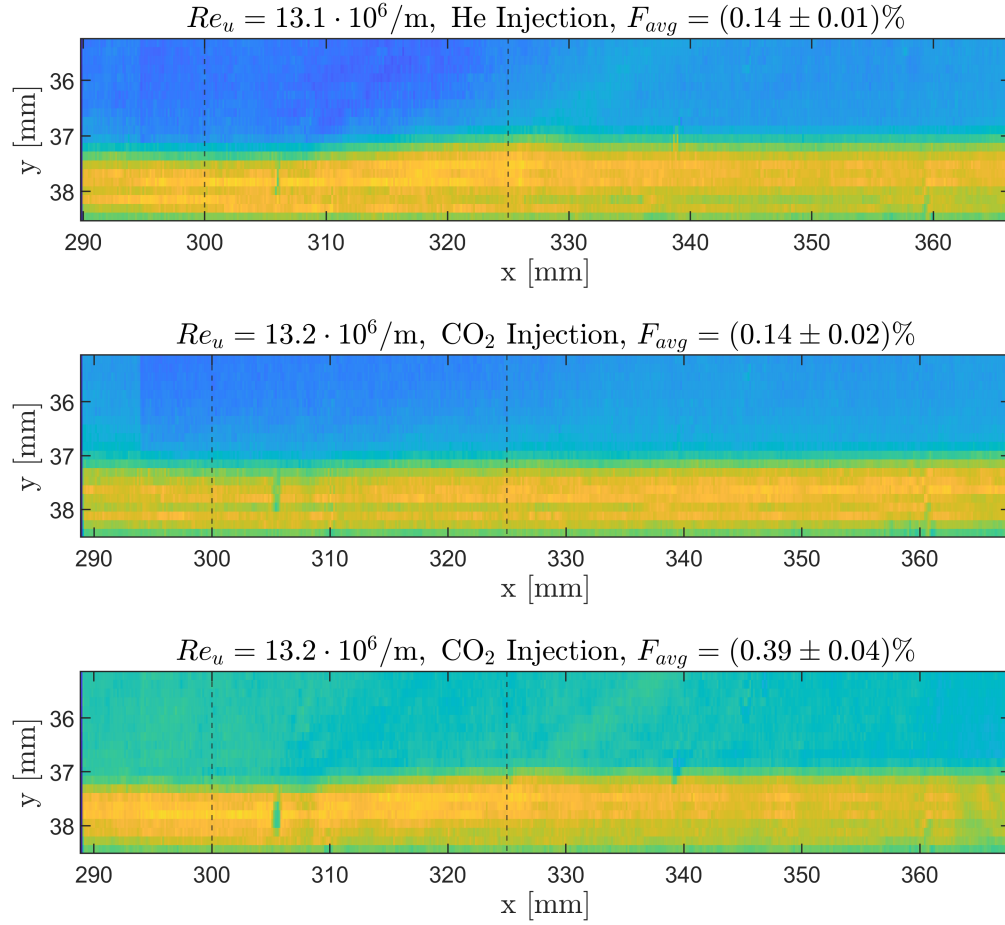


Fig. 15 Averaged schlieren images corresponding to Figure 13. Location of the injector is indicated with dashed lines.

References

- [1] Ambrose, R. F., and Greene, S., “Four Challenges to Hypersonics,” 2022. URL <https://www.lockheedmartin.com/en-us/capabilities/space/executive-blog-rick-ambrose-scott-greene-lmiq.html>, accessed: 2022 - 05 - 02.
- [2] Anderson, J. D., *Hypersonic and high temperature gas dynamics*, second edition ed., American Institute of Aeronautics and Astronautics Education Series, 2006.
- [3] Demetriades, A., “Hypersonic viscous flow over a slender cone. III-Laminar instability and transition,” *7th Fluid and PlasmaDynamics Conference*, 1974, p. 535.
- [4] Wartemann, V., Camillo, G. P., Reiter, P., Neumann, J., and Wagner, A., “Influence of transpiration cooling on second-mode instabilities investigated on hypersonic, conical flows,” *CEAS Space Journal*, 2019, pp. 1–10.
- [5] Marvin, J. G., and Akin, C. M., “Combined effects of mass addition and nose bluntness on boundary-layer transition,” *AIAA Journal*, Vol. 8, No. 5, 1970, pp. 857–863.
- [6] Mack, L. M., “Boundary-layer linear stability theory,” 1984.
- [7] Schneider, S. P., “Hypersonic boundary-layer transition with ablation and blowing,” *Journal of Spacecraft and Rockets*, Vol. 47, 2010, pp. 225–237.
- [8] Jewell, J. S., “Boundary-layer transition on a slender cone in hypervelocity flow with real gas effects,” Ph.D. thesis, 2014.
- [9] Jewell, J., Wagnild, R., Leyva, I., Candler, G., and Shepherd, J., “Transition within a hypervelocity boundary layer on a 5-degree half-angle cone in air/CO₂ mixtures,” *51st AIAA Aerospace Sciences Meeting Including the New Horizons Forum and Aerospace Exposition*, 2013, p. 523.
- [10] Wagnild, R., Candler, G., Leyva, I., Jewell, J., and Hornung, H., “Carbon dioxide injection for hypervelocity boundary layer stability,” *48th AIAA Aerospace Sciences Meeting Including the New Horizons Forum and Aerospace Exposition*, 2010, p. 1244.
- [11] Leyva, I., Laurence, S., Beierholm, A., Hornung, H., Wagnild, R., and Candler, G., “Transition delay in hypervelocity boundary layers by means of CO₂/acoustic instability interactions,” *47th AIAA Aerospace Sciences Meeting Including the New Horizons Forum and Aerospace Exposition*, 2009, p. 1287.
- [12] Camillo, G. P., Wagner, A., Dittert, C., Benjamin, L., Wartemann, V., Neumann, J., and Hink, R., “Experimental investigation of the effect of transpiration cooling on second mode instabilities in a hypersonic boundary layer,” *Experiments in Fluids*, Vol. 61, 2020, pp. 1–19.
- [13] Miró, F. M., Dehairs, P., Pinna, F., Gkolias, M., Masutti, D., Regert, T., and Chazot, O., “Effect of Wall Blowing on Hypersonic Boundary-Layer Transition,” *AIAA Journal*, Vol. 57, 2019, pp. 1567–1578.
- [14] Miró, F. M., and Pinna, F., “Injection-gas-composition effects on hypersonic boundary-layer transition,” *Journal of Fluid Mechanics*, Vol. 890, 2020.
- [15] Portec, “Metapore Porous Materials,” 2. URL <https://www.portec.ch/products/metapor-block-material>.
- [16] Wylie, S., and McGilvray, M., “HIFiRE-1 Post-Flight Experiments in the University of Oxford’s High Density Tunnel,” *AIAA Scitech 2019 Forum*, 2019, p. 1940.
- [17] Grossir, G., “Longshot hypersonic wind tunnel flow characterization and boundary layer stability investigations,” Ph.D. thesis, von Karman Institute for Fluid Dynamics-Université Libre de Bruxelles, 2015.
- [18] Casper, K., Beresh, S., Henfling, J., Spillers, R., Pruett, B., and Schneider, S., “Hypersonic wind-tunnel measurements of boundary-layer pressure fluctuations,” *39th AIAA fluid dynamics conference*, 2009, p. 4054.
- [19] Estorf, M., Radespiel, R., Schneider, S., Johnson, H., and Hein, S., “Surface-pressure measurements of second-mode instability in quiet hypersonic flow,” *46th AIAA Aerospace Sciences Meeting and Exhibit*, 2008, p. 1153.
- [20] Inc., O. E., “Mass Flow Controllers with 20+ Gas Select Functions,” 2022. URL https://www.omega.co.uk/pptst/FMA2600_FVL2600.html.
- [21] Pappas, C. C., and Okuno, A. F., *Heat-transfer measurement for binary gas laminar boundary layers with high rates of injection*, Vol. 2473, National Aeronautics and Space Administration, 1964.

- [22] Rocher, M. E., McGilvray, M., Hermann, T. A., Ifti, H. S., Hufgard, F., Eberhart, M. F., Meindl, A., Loehle, S., Giovannini, T., and Vandeperre, L. J., "Testing a transpiration cooled zirconium-di-boride sample in the plasma tunnel at IRS," *AIAA Scitech 2019 forum*, 2019, p. 1552.
- [23] Taylor, G. I., and Maccoll, J. W., "The air pressure on a cone moving at high speeds.—II," *Proceedings of the Royal Society of London. Series A, Containing Papers of a Mathematical and Physical Character*, Vol. 139, 1933, pp. 298–311.
- [24] Kays, W. M., *Convective heat and mass transfer*, Tata McGraw-Hill Education, 2012.
- [25] Marvin, J. G., and Pope, R. B., "Laminar convective heating and ablation in the Mars atmosphere," *AIAA Journal*, Vol. 5, 1967, pp. 240–248. <https://doi.org/10.2514/3.3948>.
- [26] Eckert, E. R., "Survey of boundary layer heat transfer at high velocities and high temperatures," Tech. rep., MINNESOTA UNIV MINNEAPOLIS HEAT TRANSFER LAB, 1960.
- [27] Chilton, T. H., and Colburn, A. P., "Mass transfer (absorption) coefficients prediction from data on heat transfer and fluid friction," *Industrial and engineering chemistry*, Vol. 26, 1934, pp. 1183–1187.
- [28] Keyes, F. G., "The Heat Conductivity, Viscosity, Specific Heat and Prandtl Numbers for Thirteen Gases." Tech. rep., MASSACHUSETTS INST OF TECH CAMBRIDGE, 1952.
- [29] Sutherland, W., "LII. The viscosity of gases and molecular force," *The London, Edinburgh, and Dublin Philosophical Magazine and Journal of Science*, Vol. 36, 1893, pp. 507–531.
- [30] Driest, E. R. V., *The problem of aerodynamic heating*, Institute of the Aeronautical Sciences, 1956.
- [31] Mangler, W., "Zusammenhang zwischen ebenen und rotationssymmetrischen Grenzschichten in kompressiblen Flüssigkeiten," *ZAMM-Journal of Applied Mathematics and Mechanics/Zeitschrift für Angewandte Mathematik und Mechanik*, Vol. 28, 1948, pp. 97–103.
- [32] Ifti, H. S., Hermann, T., and McGilvray, M., "Flow characterisation of transpiring porous media for hypersonic vehicles," *22nd AIAA International Space Planes and Hypersonics Systems and Technologies Conference*, 2018. <https://doi.org/10.2514/6.2018-5167>.
- [33] Rocher, M. E., Hermann, T., McGilvray, M., Ifti, H. S., Vieira, J., Hambidge, C., Quinn, M. K., Grossman, M., and Vandeperre, L., "Pressure-sensitive paint diagnostic to measure species concentration on transpiration-cooled walls," *Experiments in Fluids*, Vol. 63, 2021, p. 2. <https://doi.org/10.1007/s00348-021-03355-9>, URL <https://doi.org/10.1007/s00348-021-03355-9>.
- [34] Nelder, J. A., and Mead, R., "A simplex method for function minimization," *The computer journal*, Vol. 7, No. 4, 1965, pp. 308–313.
- [35] Lagarias, J. C., Reeds, J. A., Wright, M. H., and Wright, P. E., "Convergence properties of the Nelder–Mead simplex method in low dimensions," *SIAM Journal on optimization*, Vol. 9, No. 1, 1998, pp. 112–147.
- [36] Wylie, S., Doherty, L., and McGilvray, M., "Commissioning of the Oxford high density tunnel (HDT) for boundary layer instability measurements at Mach 7," *2018 Fluid Dynamics Conference*, 2018, p. 3074.
- [37] McGilvray, M., Doherty, L. J., Morgan, R. G., Gildfind, D., Jacobs, P., and Ireland, P., "T6: The Oxford University Stalker Tunnel," *20th AIAA International Space Planes and Hypersonic Systems and Technologies Conference*, 2015, p. 3545.
- [38] Welch, P., "The use of fast Fourier transform for the estimation of power spectra: a method based on time averaging over short, modified periodograms," *IEEE Transactions on audio and electroacoustics*, Vol. 15, 1967, pp. 70–73.
- [39] Stoica, P., and Moses, R. L., "Spectral analysis of signals," 2005.
- [40] Hann, J. V., *Handbook of climatology*, MacMillan, 1903.
- [41] Oppenheim, A. V., *Discrete-time signal processing*, Pearson Education India, 1999.
- [42] Morris, A., "Charaterisation of a novel field asymmetric ion mobility spectrometer and its evaluation for non-traditional applications," Ph.D. thesis, The Open University, 2011.
- [43] Lindner, R. R., Vera-Ciro, C., Murray, C. E., Stanimirović, S., Babler, B., Heiles, C., Hennebelle, P., Goss, W., and Dickey, J., "Autonomous gaussian decomposition," *The Astronomical Journal*, Vol. 149, No. 4, 2015, p. 138.

- [44] Bell, K., “Fitting features in a power spectrum with least squares and MLE,” <http://keatonb.github.io/archivers/powerspectrumfits>, 2018. Accessed: 2022-05-01.
- [45] Jones, E., Oliphant, T., Peterson, P., et al., “SciPy: Open source scientific tools for Python,” , 2001–. URL <http://www.scipy.org/>.
- [46] Span, R., “D2. 2 Properties of Dry Air,” *VDI-GVC, Ed. VDI Heat Atlas. 2nd Ed*, Springer Berlin Heidelberg, 2010, pp. 172–191.
- [47] Ifiti, H. S., “Transpiration Cooling of a Hypersonic Vehicle,” Ph.D. thesis, Wolfson College, University of Oxford, 2021.
- [48] Ifiti, H. S., “Analytical Model of Wall Coolant Concentration Downstream of a Transpiration-Cooled Injector in a Laminar Boundary-Layer,” *Journal of Fluid Mechanics*, 2022. Manuscript submitted for publication.
- [49] Anderson, J. D., *Modern compressible flow: with historical perspective*, Vol. 12, McGraw-Hill New York, 1990.
- [50] Schmidt, B. E., and Shepherd, J., “Measurements of instability in supersonic flow with injection by time-resolved flow visualization,” *54th AIAA Aerospace Sciences Meeting*, 2016, p. 0599.
- [51] Schmidt, B. E., Bitter, N. P., Hornung, H. G., and Shepherd, J. E., “Injection into supersonic boundary layers,” *AIAA Journal*, Vol. 54, 2016, pp. 161–173.
- [52] Schardin, H., “Das toepplersche schlierenverfahren: Grundlagen fur seine anwendung und quantitative auswertung,” *VDI Forschungsheft*, Vol. 367, 1934, pp. 1–32.
- [53] Settles, G. S., *Schlieren and shadowgraph techniques: visualizing phenomena in transparent media*, Springer Science & Business Media, 2012.
- [54] Schardin, H., “Die schlierenverfahren und ihre anwendungen,” *Ergebnisse der exakten Naturwissenschaften*, 1942, pp. 303–439.
- [55] Laurence, S. J., Wagner, A., and Hannemann, K., “Experimental study of second-mode instability growth and breakdown in a hypersonic boundary layer using high-speed schlieren visualization,” *Journal of Fluid Mechanics*, Vol. 797, 2016, pp. 471–503. <https://doi.org/DOI:10.1017/jfm.2016.280>.
- [56] Trujillo-Pino, A., Krissian, K., Alemán-Flores, M., and Santana-Cedrés, D., “Accurate subpixel edge location based on partial area effect,” *Image and Vision Computing*, Vol. 31, 2013, pp. 72–90. <https://doi.org/https://doi.org/10.1016/j.imavis.2012.10.005>, URL <https://www.sciencedirect.com/science/article/pii/S0262885612001850>.
- [57] Trujillo-Pino, A., “Accurate subpixel edge location,” <https://www.mathworks.com/matlabcentral/fileexchange/48908-accurate-subpixel-edge-location>, 2022. Retrieved May 1, 2022.
- [58] Fedorov, A. V., Soudakov, V., and Leyva, I. A., “Stability analysis of high-speed boundary-layer flow with gas injection,” *7th AIAA Theoretical Fluid Mechanics Conference*, 2014, p. 2498.
- [59] Fedorov, A., “Transition and Stability of High-Speed Boundary Layers,” *Annual Review of Fluid Mechanics*, Vol. 43, 2011, pp. 79–95. <https://doi.org/10.1146/annurev-fluid-122109-160750>, URL <https://doi.org/10.1146/annurev-fluid-122109-160750>.